Original Research

Improved Myelin Water Quantification Using Spatially Regularized Non-negative Least Squares Algorithm

Dosik Hwang, PhD,[1] and Yiping P. Du, PhD[2]*

Purpose: To improve the myelin water quantification in the brain in the presence of measurement noise and to increase the visibility of small focal lesions in myelin-water-fraction (MWF) maps.

Materials and Methods: A spatially regularized non-negative least squares (srNNLS) algorithm was developed for robust myelin water quantification in the brain. The regularization for the conventional NNLS algorithm was expanded into the spatial domain in addition to the spectral domain. Synthetic data simulations were performed to study the effectiveness of this new algorithm. Experimental free-induction-decay measurements were obtained using a multi-gradient-echo pulse sequence and MWF maps were estimated using the srNNLS algorithm. The results were compared with other conventional methods.

Results: A substantial decrease in MWF variability was observed in both simulations and experimental data when the srNNLS algorithm was applied. As a result, false lesions in the MWF maps disappeared and the visibility of small focal lesions improved greatly. On average, the contrast-to-noise ratio for focal lesions was improved by a factor of 2.

Conclusion: The MWF variability due to the measurement noise can be substantially reduced and the detection of small focal lesions can be improved by using the srNNLS algorithm.

Key Words: myelin content; myelin water fraction; multiple sclerosis; non-negative least squares; regularization; multiexponential analysis.
J. Magn. Reson. Imaging 2009;30:203–208.

QUANTITATIVE MEASUREMENTS of myelin content can substantially improve our understanding of the pathological progress of several white matter (WM) diseases, such as multiple sclerosis (MS) (1–4). A technique that provides specific and sensitive information about the myelin content was developed based on an analysis of T_2 relaxation times (5,6). It has been reported that the T_2 spectrum of WM and several myelinated tissue samples consists of multiple components (7–13) and that the short component with T_2 between 10 ms and 50 ms corresponds to the water pool within the myelin sheath (2–6). Myelin content can therefore be quantitated using the fraction of this short T_2 component. To implement this method, T_2 decay signals are acquired using a 32-echo single-slice Carr-Purcell-Meiboom-Gill (CPMG) sequence with composite 90x-180y-90x refocusing pulses and big crusher gradients around the refocusing pulses (5,6,14,15). A non-negative least squares (NNLS) algorithm can then be used to estimate the T_2 spectrum from the acquired decay signal, and the myelin water fraction (MWF) can be calculated from the ratio of the short T_2 component (10 ms $< T_2 <$ 50 ms) to the total (16). A strong correlation was found between the MWF measured using this technique and the myelin distribution using histopathology in fixed brains (4,17). This technique has been used to quantitatively measure the MWF in brains of subjects with MS (3–6,17).

T_2 spectrum regularization has been applied to the NNLS algorithm to improve the reliability of fitting in the presence of noise. The regularized non-negative least squares (rNNLS) algorithm finds a T_2 spectrum that minimizes the T_2 distribution energy such that $1.02\chi^2_{min} \leq \chi^2 \leq 1.025\chi^2_{min}$ where χ^2_{min} is the minimum misfit of the unregularized NNLS solution (2,4,18,19). Despite its improved performance compared with the original NNLS algorithm, the rNNLS algorithm is still sensitive to noise in the data. Therefore, to achieve reasonable SNR before the rNNLS algorithm is applied, four CPMG acquisitions at 1.5 Tesla (T) are typically averaged, which makes the total acquisition time as long as 26 minutes for a single slice (3,4,6,18).

In this study, we expanded the regularization of the rNNLS algorithm into the spatial domain in addition to the spectral domain for robust MWF measurements with reduced sensitivity to noise. A similar spatial regularization concept was used in the analysis of longitudinal relaxation data for the inverse Laplace transform to obtain the fractional contributions of WM, gray mat-

[1]School of Electrical and Electronic Engineering, Yonsei University, Seoul, Korea.
[2]Department of Psychiatry, University of Colorado Denver, Colorado.
Contract grant sponsor: Pilot Grant, The National Multiple Sclerosis Society, USA (YPD, DH); contract grant sponsor: Yonsei Research Fund, Korea (DH); Basic research program of the Korea Science and Engineering Foundation (RO1-2008-000-20270-0) (DH).
*Address reprint requests to: Y.P.D., Brain Imaging Center, University of Colorado Denver, School of Medicine, Mail Stop F-478, PO.Box 6508, 12469 East 17th Place, BLDG 400, RM 110, Aurora, Colorado 80045. E-mail: yiping.du@ucdenver.edu
Received December 4, 2008; Accepted March 10, 2009.
DOI 10.1002/jmri.21783
Published online in Wiley InterScience (www.interscience.wiley.com).

ter (GM), and MWF maps based on the T_1 spectrum (20–22).

The spatially regularized non-negative least squares (srNNLS) algorithm is based on the assumption that the T_2 spectra among neighboring voxels have a certain degree of similarity. A priori information about the T_2 spectrum of any given voxel can be extracted from its neighbors and incorporated into the fitting procedure for robust spectrum estimation. Simulations were performed to assess the effectiveness of the srNNLS algorithm. The visibility of small lesions and the MWF variability was examined in the presence of noise. For the in vitro experiments, a multi-gradient-echo (MGRE) pulse sequence was used to acquire T_2* decay signals on a fixed MS brain. The feasibility of using T_2* decay to measure MWF has been demonstrated previously (23). MWF maps obtained using the rNNLS algorithm and the srNNLS algorithm were compared for both the simulation and in vitro experiments. Finally, the srNNLS algorithm was applied to in vivo data.

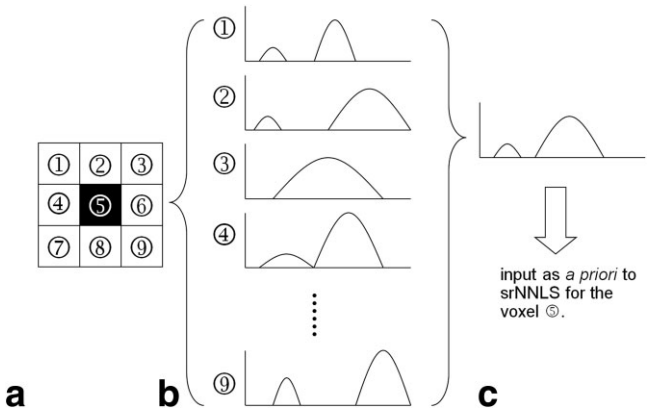

Figure 1. The diagram of the srNNLS algorithm (hypothetical illustration). **a:** Nine neighboring pixels of a part of an image, (**b**) T_2 spectrum for each pixel estimated using the rNNLS algorithm, (**c**) the estimated a priori spectrum for the pixel 5.

MATERIALS AND METHODS

Data Acquisition

A postmortem MS brain with several focal lesions was scanned with a 126-echo MGRE sequence on a 3T MRI scanner (General Electric, Waukesha, WI) with a standard head-volume coil. The brain was fixed in 10% buffered formalin for more than a year and then placed in a water-filled container for scanning after careful removal of air bubbles. High-order shim was performed to minimize the field inhomogeneity. The MGRE sequence uses a train of readout gradients with alternating polarity immediately after phase-encoding, similar to the pulse sequence used in echo-planar spectroscopic imaging (24). The echoes were acquired on both the flat-top and the readout gradient ramps to further shorten the first echo time (TE1) and echo spacing (ES). Gradient spoilers were applied to all the three axes at the end of the readout train to destroy any residual transverse component of the magnetization. The image matrix was 256 × 256, repetition time (TR) = 2 s, field of view (FOV) = 20 cm, slice thickness = 3 mm, TE1 = 2.1 ms, and ES = 1.1 ms. The scan time was 8.5 min. The acquired *k*-space data was reconstructed into the (x, y, t) domain on an off-line computer using reconstruction software developed in our lab. A T_2-FLAIR image was also obtained for comparison with the estimated MWF maps (TE/TR/TI = 126 ms / 8.8 s / 2.2 s, matrix size = 256 × 256, FOV = 20 cm, thickness = 3 mm).

For the in vivo experiment, a normal volunteer in his mid-30s was scanned with the MGRE sequence. An eight-channel phased-array coil was used and four repetitions were averaged to achieve high SNR (matrix size = 256 × 256, FOV = 24 cm, slice thickness = 4 mm, total scan time = 34 min).

Data Analysis

The T_2* spectra were estimated from the acquired free-induction-decay (FID) signals for each pixel using the rNNLS and srNNLS algorithms. The srNNLS algorithm is as follows:

$$\min_s\{\|As - y\|_2 + \mu\|Hs - p\|_2\}$$

subject to

$$s \geq 0 \qquad [1]$$

where s is the T_2* spectrum, y is the FID measurements, **A** is the system matrix which transforms the T_2* spectrum (s) into the FID signals (y) ($A_{ij} = \exp(-TE_i/T_2{*}_j)$ and $y = As$), μ is the regularization parameter, H is the weighting matrix which determines the importance (weight) of each element of s in the minimization process (the identity matrix was used for H in this study, suggesting equal weights for all elements), and p is the a priori spectrum. The expression in Eq. [1] becomes the unregularized NNLS algorithm when μ is zero, and becomes the rNNLS algorithm when μ is nonzero and p is zero. For the rNNLS algorithm, μ was selected such that $1.02\chi^2_{\min} \leq \chi^2 \leq 1.025\chi^2_{\min}$ where $\chi^2_{\min}$ is the minimum misfit of the unregularized NNLS solution. Once the spectra for all pixels were obtained using the rNNLS algorithm, p was estimated and then the final spectrum was obtained for each pixel using the srNNLS algorithm (Eq. [1]). The diagram in Figure 1 illustrates the srNNLS algorithm. Figure 1a shows nine neighboring pixels of a part of an image. For each pixel, the T_2* spectrum is estimated by the rNNLS algorithm as illustrated in Figure 1b. The variation of the spectra from one pixel to another may be large due to the noise in FID signals, resulting in an increase of MWF variability and spatial noise in the MWF map. This variation can be reduced by constraining each spectrum in the spatial domain. The average of nine spectra in Figure 1b was used as the a priori spectrum p in Eq. [1] for the final estimation of the spectrum for pixel 5 (Fig. 1c). The value of μ was selected to keep a level of regularization similar to that of the rNNLS algorithm.

Simulation of Synthetic Data

Simulations with synthetic image data were performed to assess MWF variability and the visibility of small

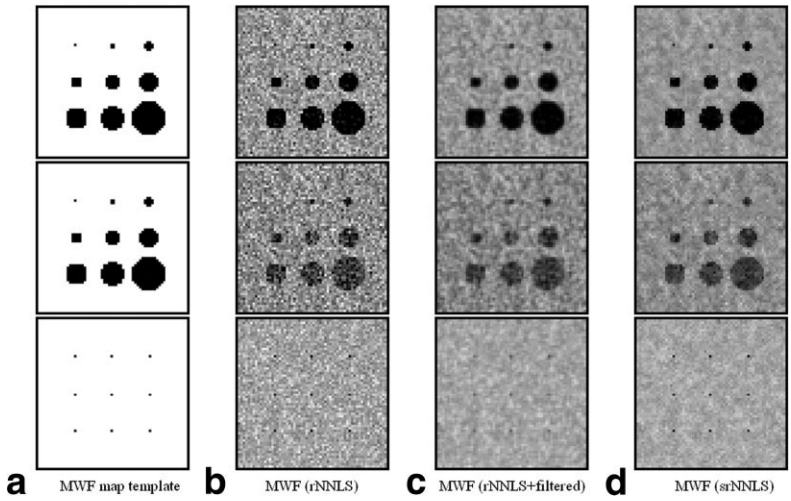

Figure 2. a–d: Simulation studies. The background represents WM (MWF = 15%). The dark circles represent MS lesions. Top row: SNR = 100, MWF of lesions = 0%. Middle row: SNR = 70, MWF of lesions = 7.5%. Bottom row: SNR = 150, MWF of lesions = 3%. The MWF maps estimated using the srNNLS algorithm show the greatest visibility of small lesions with a substantial reduction of spatial noise.

lesions in the presence of noise. Three synthetic datasets with different SNRs and contrasts were used in the simulations. Figure 2a shows the synthetic images in which the background represents a normal WM and the black circles represent MS lesions. The radius of lesions varied from 0.5 to 7 pixels. The smallest lesion had the size of a single pixel. Each pixel in the synthetic images had a T_2^* spectrum which consisted of two main peaks at 7 ms and 60 ms, with the short T_2^* component representing the myelin water and the long T_2^* component representing the intra/extracellular water. MWF was defined as the ratio of the signal in the T_2^* distribution 3 ms $\leq T_2^* \leq$ 16 ms to the total signal. The MWF of the normal WM was set to be 15%. The MWF of the lesions varied from 0 to 7.5%. The FID signal consisted of 126 echoes. TE1 was 2.1 ms and ES was 1.1 ms. Gaussian noise was added to the FID signals to reach three different SNR values (70, 100, 150) at TE1. The FID signals from each dataset were fitted using the rNNLS algorithm and the srNNLS algorithm to estimate the T_2^* spectrum and determine MWF. The MWF maps estimated using these two methods were visually compared and contrast-to-noise ratios (CNR) for small focal lesions were examined. CNR was defined as follows: $CNR = | MWF_{lesion} - MWF_{WM} | / SD_{WM}$, where MWF_{lesion} is the MWF value of the single-pixel lesion, MWF_{WM} is the mean MWF of the surrounding WM (eight pixels), and SD_{WM} is the standard deviation of the MWF of the surrounding WM. In addition, the MWF maps estimated using the rNNLS algorithm were filtered using a spatial low-pass filter (Gaussian with a standard distribution of 0.6 pixels) and compared with the maps estimated using the srNNLS algorithm. We performed this comparison to illustrate how effective the srNNLS algorithm is at reducing spatial noise and improving the visibility of small lesions without compromising spatial resolution.

RESULTS

Figure 2 shows (a) the MWF map template for the synthetic data, (b) the MWF maps estimated using the rNNLS algorithm (MWF_{rNNLS}), (c) their low-pass filtered images ($MWF_{rNNLS,filtered}$), and (d) the MWF maps estimated using the srNNLS algorithm (MWF_{srNNLS}), from the left to the right column, respectively. The top row shows the estimated MWF maps from the synthetic data in which SNR = 100 and the MWF of lesions = 0% (the intensity of the first peak (at 7 ms) in the T_2^* spectrum was set to zero for the lesions). The MWF_{rNNLS} map contains high spatial noise and the smallest lesion (a single-pixel lesion) is not conspicuous. In the low-pass filtered map, the spatial noise was reduced, but the smallest lesion was still not conspicuous and the edges of other lesions were smoothed. In contrast, the MWF_{srNNLS} map showed improved small lesion visibility and sharp edges with a substantial noise reduction. The middle row shows the estimated MWF maps from the synthetic data in which SNR = 70 and the MWF of lesions = 7.5% (the intensity of the first peak at 7 ms in the T_2^* spectrum was rescaled such that the MWF of the pixels in the lesions was 0.075). The overall noise level in the MWF maps was higher and the contrast was reduced compared with the top row. The smallest lesion was not detectable in any of the three maps. The original shapes and edges of lesions were best represented in the MWF_{srNNLS} map. More quantitatively, the similarity in shape between the original lesions and those estimated based on MWF maps was measured using correlation coefficients (25) (Table 1). On average, the

Table 1
Correlation Coefficients Between the Original Lesions and the Estimated Ones

Lesions	1	2	3	4	5	6	7	8	9	Average
rNNLS	0.176	0.759	0.787	0.823	0.715	0.769	0.759	0.742	0.750	0.698
rNNLS+filtered	0.205	0.773	0.863	0.865	0.837	0.875	0.875	0.885	0.882	0.784
srNNLS	0.580	0.810	0.932	0.897	0.877	0.920	0.917	0.914	0.919	0.863

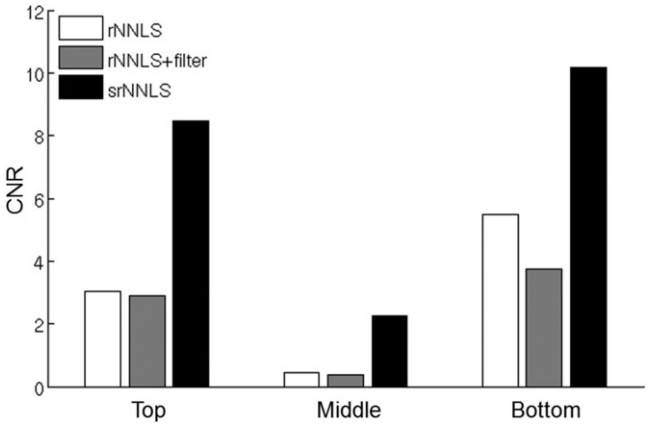

Figure 3. Contrast-to-noise ratio (CNR) for the single-pixel lesions in simulations (top, middle, and bottom rows in Fig. 2). The CNR was substantially improved when MWF was measured using the srNNLS algorithm, compared with the rNNLS algorithm. The spatial low-pass filtering did not improve the CNR.

correlation coefficients were 0.698, 0.784, and 0.863 for the rNNLS, rNNLS+filtered, and srNNLS algorithms, respectively. The bottom row shows the estimated MWF maps from the synthetic data in which SNR = 150 and the MWF of lesions = 3% (the intensity of the first peak at 7 ms in the T_2* spectrum was rescaled such that the MWF of the lesions was 0.03). All single-pixel lesions were identifiable in all three maps, but the MWF_{srNNLS} map showed the highest visibility of the lesions. The graph in Figure 3 shows the CNR differences among the three different MWF maps. The CNR was measured between the single-pixel lesion and its surrounding WM pixels for all MWF maps. The CNR improved substantially when MWF was measured using the srNNLS algorithm compared with the rNNLS algorithm. Spatial low-pass filtering did not improve the CNR for these single-pixel lesions.

Figure 4 shows the results of the postmortem MS brain studies: (a) T_2-FLAIR image, (b) MWF_{rNNLS} map, and (c) MWF_{srNNLS} map at the same slice location of the fixed MS brain. The calculation time for the 256 × 256 MWF maps was 5.4 h and 7.1 h for the rNNLS and srNNLS algorithms, respectively (Intel Core™2 Duo CPU T7300 at 2.0 GHz, 2 GB of RAM). Seven focal lesions are indicated by arrows. The myelin water signal was well detected in regions of normal-appearing WM in both MWF maps. The MWF was substantially reduced at the locations of focal MS lesions and regions of GM. The MWF_{rNNLS} map, however, contains high spatial noise and the visibility of small lesions was reduced considerably. This type of spatial noise in the MWF map was previously described by Jones et al (18) as artifactual "holes," because they might be mistaken for small lesions. Some small lesions were barely differentiable from these "holes" in the MWF_{rNNLS} map. In contrast, this hole-type noise was substantially reduced in the MWF_{srNNLS} map, and small lesions had improved visibility. The shapes and sizes of several lesions indicated by arrows in the T_2-FLAIR image are well depicted in this map. The edges of lesions and WM are also well preserved in the MWF_{srNNLS} map. The correlation coefficients were also measured between the lesions in the T_2-FLAIR image and those in the MWF maps (Table 2). On average, the correlation coefficients were 0.544 and 0.804 for the rNNLS and srNNLS algorithms, respectively. The graph in Figure 5 shows the CNR difference between the MWF_{rNNLS} map and the MWF_{srNNLS} map. CNRs were measured on seven focal lesions indicated by arrows in Figure 4a. The ROIs for the inside/outside of lesions were drawn manually (the numbers of pixels inside/outside of lesions were 5/37, 4/20, 13/82, 18/87, 7/50, 28/88, and 20/63 for the lesions 1 ~ 7, respectively). The CNR improved substantially in all lesions when MWF was measured using the srNNLS algorithm, compared with that of the rNNLS algorithm. On average, the CNR improved by a factor of 2.14.

Table 2
Correlation Coefficients Between the Lesions in the T_2-FLAIR Image and the Estimated Ones

Lesions	1	2	3	4	5	6	7	Average
rNNLS	0.591	0.438	0.577	0.579	0.338	0.579	0.656	0.544
srNNLS	0.890	0.726	0.766	0.795	0.782	0.741	0.844	0.804

Figure 6 shows several MWF maps with different μ values: $\mu_{(srNNLS)} = \alpha\mu_{(rNNLS)}$, where α = 2, 4, 10, 15, 20, 30, 40, and 50. The MWF map with α = 2 still contains many "holes" and small lesions are not clearly visible. On maps with α = 15 and 20, several small focal lesions are clearly visible with sharp WM and GM boundaries. Lesions are still visible on the maps with α of 30, 40, and 50, but there is a blurring effect throughout the images. The CNRs of seven focal lesions were measured with different α values to find the optimal α, as shown in

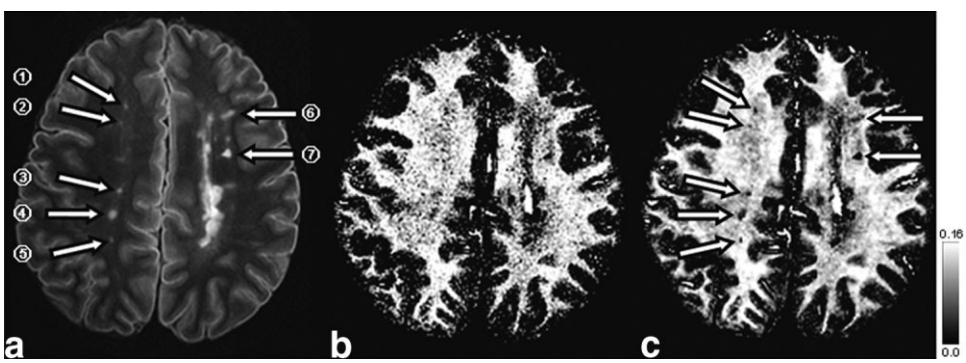

Figure 4. In vitro experiments. T_2-FLAIR image (**a**), MWF_{rNNLS} (**b**), MWF_{srNNLS} (**c**) for a fixed MS brain. Several focal MS lesions are indicated by arrows. MWF_{rNNLS} contains high spatial noise and the visibility of small focal lesions is low. MWF_{srNNLS} shows an improved visibility of lesions with a substantial reduction of spatial noise.

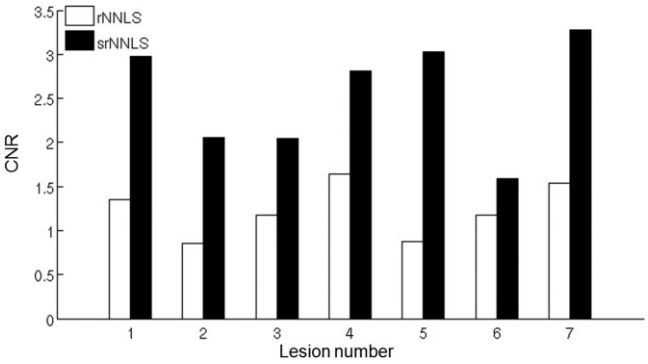

Figure 5. CNR for the MS lesions of the fixed brain. On average, the CNR was improved by a factor of 2 when MWF was measured using the srNNLS algorithm, compared with the rNNLS algorithm.

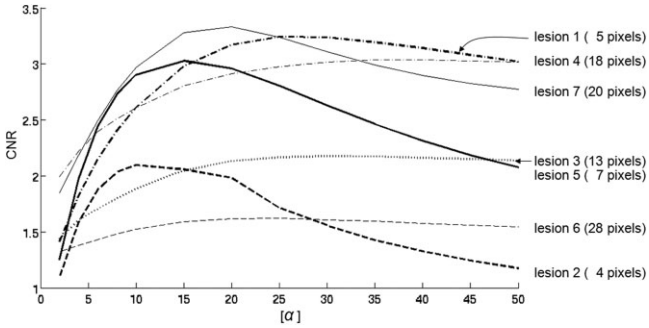

Figure 7. Effect of regularization strength: CNR of focal lesions with different regularization strength, $\mu_{(srNNLS)} = \alpha\mu_{(rNNLS)}$. The CNR's of large lesions (lesion 3 and 6) slowly increased and reached their plateaus around $\alpha = 20 \sim 25$. The CNR's of small lesions (lesion 2 and 5) reached their maxima around $\alpha = 10 \sim 15$, and kept decreasing as α increased further. The optimal range of α can be found between 15 and 20.

Figure 7. The CNRs of large lesions (lesion 3 and 6) slowly increased and reached their plateaus around $\alpha = 20 \sim 25$. The CNRs of small lesions (lesion 2 and 5) reached their maxima around $\alpha = 10 \sim 15$ and kept decreasing as α increased further. The optimal range of α can be found between $\alpha = 15$ and 20.

Figure 8 shows MWF maps from the in vivo experiments. The MWF_{rNNLS} map (b) contains high spatial noise and many "holes." In contrast, this hole-type noise was substantially reduced in the MWF_{srNNLS} map (c).

DISCUSSION

Our results demonstrate that the srNNLS algorithm can produce robust MWF measurements. The MWF variability decreased substantially with the use of the srNNLS algorithm compared with that using the rNNLS algorithm, in both simulations and the analysis of in vitro and in vivo MGRE data. This decrease in MWF variability resulted in the reduction of spatial noise in the MWF map and increased small MS lesion visibility.

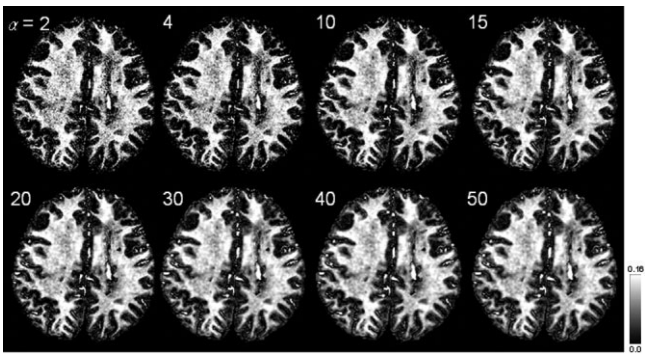

Figure 6. Effect of regularization strength, $\mu_{(srNNLS)} = \alpha\mu_{(rNNLS)}$, where $\alpha = 2$, 4, 10, 15, 20, 30, 40, and 50. The MWF map with $\alpha = 2$ still contains many "holes" and the visibility of small lesions is low. The MWF maps with $\alpha = 15$ and 20 show an improved visibility of several small focal lesions with sharp boundaries of WM and GM. The maps with $\alpha = 30$, 40, and 50 still show reasonable visibility of lesions but have introduced blurring effect throughout the images.

Conventional low-pass spatial filters reduced the noise, at the expense of increased blurring and reduced visibility of small lesions. In contrast, the srNNLS algorithm effectively reduced the spatial noise, improved the visibility of small focal lesions, and preserved sharp boundaries of lesions and WM in the MWF maps.

An edge-preserving nonlinear filter has also been used to reduce noise in MWF maps. Nonlinear filters such as median filter and anisotropic diffusion filter (ADF) are known to be effective in reducing noise while preserving sharp edges. However, they also tend to introduce artifacts such as flat zones and boundaries inside smooth regions (26,27). In our preliminary studies (data not shown), the application of ADF successfully reduced many false "holes" without compromising spatial resolution as previously demonstrated in Jones et al (18). However, a certain degree of unnatural appearance (flat zones and boundaries) was observed in the MWF map. For applications in which this type of unnatural appearance is unimportant, the srNNLS algorithm could be combined with ADF to further reduce the noise. We observed that noise along the boundaries of WM and GM that was present in the $MWF_{ADF+rNNLS}$ map, was substantially reduced in the $MWF_{ADF+srNNLS}$

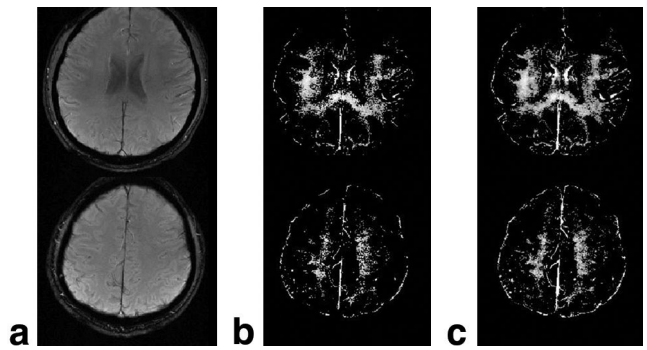

Figure 8. In vivo experiment. Anatomical images at TE = 17.4 ms (**a**), MWF_{rNNLS} (**b**), MWF_{srNNLS} (**c**) for a living brain. MWF_{rNNLS} contains high spatial noise and many "holes." This hole-type noise has been substantially reduced in MWF_{srNNLS}.

map leading to clean, sharp, and continuous edges. The visibility of focal lesions was also improved.

The regularization parameter (μ) should be carefully chosen for optimal performance. If μ is too low, the srNNLS algorithm will not produce better MWF maps than the rNNLS algorithm. If μ is too high, excessive blurring will be introduced to the MWF map. In the current implementation of the srNNLS algorithm, μ was selected to ensure a similar regularization strength to that in the rNNLS algorithm. In the rNNLS algorithm, μ was chosen to meet the previously described criteria, $1.02\chi^2_{min} \leq \chi^2 \leq 1.025\chi^2_{min}$, which maintains a balance between the first ($\|As - y\|_2$) and second ($\|Hs - p\|_2$) terms of Eq. [1] in the minimization process. To keep a similar regularization strength in the srNNLS algorithm, different values of μ should be used because p is nonzero in the srNNLS algorithm. In the simulations, the ratio of the second term of Eq. [1] in the rNNLS algorithm to that of the srNNLS algorithm, $\|Hs - 0\|_2$ / $\|Hs - p\|_2$, was approximately 10. Therefore, a new μ value, $\mu_{(srNNLS)} = 10\ \mu_{(rNNLS)}$ was used in the analyses of the synthetic and experimental data in our study.

The srNNLS algorithm also performed better than the rNNLS algorithm when applied to in vivo data. Hole-type noise was substantially reduced in MWF_{srNNLS} maps.

A more sophisticated method to estimate the a priori spectrum, p, needs further investigation. In the current implementation of the srNNLS algorithm, p was calculated by averaging the spectra of nine neighboring pixels estimated using the rNNLS algorithm. The optimal range of neighbors and the corresponding weighting scheme may lead to a better estimation of the a priori spectrum, which in turn would produce a better MWF estimation. Expansion of the regularization into the z direction, resulting in a four-dimensional regularization (x-y-z-T_2*), may further improve the estimation of the a priori spectrum. In this case, the z resolution needs to be commensurate with the in-plane resolution or an appropriate weighting scheme should be developed.

In conclusion, this study demonstrates that spatial regularization of the NNLS algorithm can substantially reduce spatial noise in MWF measurements and improve the visibility of small focal lesions in MWF maps.

ACKNOWLEDGMENTS

The authors thank the anonymous reviewer for bringing Dr. Labadie's previous work to their attention, and Dr. Jack H. Simon for his insightful discussion. This work was funded by a pilot grant from the National Multiple Sclerosis Society. USA.

REFERENCES

1. Miller DH, Grossman RI, Reingold SC, McFarland HF. The role of magnetic resonance techniques in understanding and managing multiple sclerosis. Brain 1998;121:3–24.
2. MacKay A, Laule C, Vavasour I, Bjarnason T, Kolind S, Madler B. Insights into brain microstructure from the T2 distribution. Magn Reson Imaging 2006;24:515–525.
3. Laule C, Vavasour IM, Moore GR, et al. Water content and myelin water fraction in multiple sclerosis: a T2 relaxation study. J Neurol 2004;251:284–293.
4. Laule C, Leung E, Li DK, et al. Myelin water imaging in multiple sclerosis: quantitative correlations with histopathology. Mult Scler 2006;12:747–753.
5. MacKay A, Whittall K, Adler J, Li D, Paty D, Graeb D. In vivo visualization of myelin water in brain by magnetic resonance. Magn Reson Med 1994;31:673–677.
6. Whittall KP, MacKay AL, Graeb DA, Nugent RA, Li DKB, Paty DW. In vivo measurement of T2 distributions and water contents in normal human brain. Magn Reson Med 1997;37:34–43.
7. Peled S, Cory DG, Raymond SA, Kirschner DA, Jolesz FA. Water diffusion, T2, and compartmentation in frog sciatic nerve. Magn Reson Med 1999;42:911–918.
8. Does MD, Gore JC. Compartmental study of T1 and T2 in rat brain and trigeminal nerve in vivo. Magn Reson Med 2002;47:274–283.
9. Wachowicz K, Snyder RE. Assignment of the T2 components of amphibian peripheral nerve to their microanatomical compartments. Magn Reson Med 2002;47:239–245.
10. Lancaster JL, Andrews T, Hardies LJ, Dodd S, Fox PT. Three-pool model of white matter. J Magn Reson Imaging 2003;17:1–10.
11. Andrews T, Lancaster JL, Dodd S, Contreras-Sesvold C, Fox PT. Testing the three-pool white matter model adapted for use with T2 relaxometry. Magn Reson Med 2005;54:449–454.
12. Andrews TJ, Osborne MT, Does MD. Diffusion of myelin water. Magn Reson Med 2006;56:381–385.
13. Valentine HL, Does MD, Marshall V, Tonkin EG, Valentine WM. Multicomponent T2 analysis of dithiocarbamate-mediated peripheral nerve demyelination. Neurotoxicology 2007;28:645–654.
14. Levitt MH, Freeman R. NMR population inversion using a composite pulse. J Magn Reson 1979;33:473.
15. Poon CS, Henkelman RM. Practical T2 quantitation for clinical applications. J Magn Reson Imaging 1992;2:541–553.
16. Whittall KP, MacKay AL. Quantitative interpretation of NMR relaxation data. J Magn Reson 1989;84:134–152.
17. Moore GRW, Leung E, MacKay AL, et al. A pathology-MRI study of the short-T2 component in formalin-fixed multiple sclerosis brain. Neurology 2000;55:1506–1510.
18. Jones CK, Whittall KP, MacKay AL. Robust myelin water quantification: averaging vs. spatial filtering. Magn Reson Med 2003;50:206–209.
19. Oh J, Han ET, Pelletier D, Nelson SJ. Measurement of in vivo multi-component T2 relaxation times for brain tissue using multi-slice T2 prep at 1.5 and 3 T. Magn Reson Imaging 2006;24:33–43.
20. Labadie C, Möller H, Jarchow S. Cross-regularisation of the frequency domain enables high-resolution inverse Laplace transform of human brain single voxel spectroscopy at 3 Tesla. In: Proceedings of the 13th Annual Meeting of ISMRM, Miami, Florida, 2005. (abstract 56).
21. Labadie C, Jarchow S, Möller HE. Estimation of fractional contributions of white and gray matter by cross-regularized inverse Laplace transform. In: Proceedings of the Joint Annual Meeting of ISMRM-ESMRMB, Berlin, Germany, 2007. (abstract 2106).
22. Labadie C, Lee JH, Jarchow S, Rooney WD, Springer CS, Möller HE. Detection of the myelin water fraction in 4 Tesla longitudinal relaxation data by cross-regularized inverse Laplace transform. In: Proceedings of the 16th Annual Meeting of ISMRM, Toronto, Canada, 2008. (abstract 2243).
23. Du YP, Chu R, Hwang D, et al. Fast multislice mapping of the myelin water fraction using multicompartment analysis of T2* decay at 3T: a preliminary postmortem study. Magn Reson Med 2007;58:865–870.
24. Posse S, Dager SR, Richards TL, et al. In vivo measurement of regional brain metabolic response to hyperventilation using magnetic resonance: proton echo planar spectroscopic imaging (PEPSI). Magn Reson Med 1997;37:858–865.
25. Rodgers JL, Nicewander WA. Thirteen ways to look at the correlation coefficient. Am Stat 1988;42:59–66.
26. Gerig G, Kubler O, Kikinis R, Jolesz F. Nonlinear anisotropic filtering of MRI data. IEEE Trans Med Imaging 1992;11:221–231.
27. Buades A, Coll B, Morel JM. The staircasing effect in neighborhood filters and its solution. IEEE Trans Image Process 2006;15:1499–1505.